Establishing design principles for emissive organic SWIR chromophores from energy gap laws

*Hannah C. Friedman, Emily D. Cosco, Timothy L. Atallah, Shang Jia, Ellen M. Sletten, Justin R. Caram**

Department of Chemistry and Biochemistry, University of California, Los Angeles, 607 Charles E. Young Drive, Los Angeles, California 90095-1569, United States

Abstract: Rational design of bright near and shortwave infrared (NIR: 700–1000 SWIR: 1000–2000 nm) molecular and nanoscale emitters is a fundamental scientific question with applications ranging from deep tissue imaging to new photonic materials. However, all reported organic chromophores with energy gaps in the SWIR have very low quantum yields. Is there a fundamental limit for the quantum yield of organic chromophores in the SWIR? Here we combine experiment and theory to derive an energy gap quantum yield master equation (EQME), which describes the fundamental limits in SWIR quantum yields for organic chromophores in terms of energy gap laws for radiative and nonradiative decay. We parametrize EQME using experimental data from time-correlated single photon counting in the SWIR acquired using superconducting nanowire single photon detectors operating beyond the bandgap of silicon. Evaluating the photophysics of 21 polymethine NIR/SWIR emissive chromophores, we explain the precipitous decline of ϕ_F past 900 nm as the result of decreased radiative rates and increased nonradiative deactivation via high frequency vibrations as a function of singlet energy gap. From EQME we can compare quantum yields among NIR/SWIR chromophores while accounting for changes in energy gaps. We find that electron donating character on polymethine heterocycles results in relative increases in radiative efficiency obscured by a simultaneous redshift. We correlate the improved relative

quantum yield to changes in transition dipole moments across the chromenylium polymethine family. Finally, understanding energy gap laws reveals quantitative estimates the effect of deuteration or molecular aggregation as strategies to increase ϕ_F in the SWIR. We experimentally demonstrate that partial deuteration of the chromophore Flav7 results in decreased nonradiative rates and concomitant increases in quantum yield. These insights will enable optimal chromophore designs for SWIR fluorescence.

Introduction: Shortwave infrared (SWIR, or NIR-II/III, ~1000–2000 nm) radiation offers imaging capabilities with superlative contrast and feature resolution. Reflective and fluorescent imaging in the SWIR has been shown to enable penetrative imaging—through fog, foliage, skin and bone,[1–3] enabling broad applications ranging from image-guided surgery to self-driving cars.[4–7] The SWIR spectral region has lower background due to few natural sources of radiation (e.g. blackbody radiation, tissue autofluorescence), compared to the visible (VIS, 350–700 nm) and near-infrared (NIR, 700–1000) regions. Expanding and improving the library of bright SWIR chromophores that can sense biological, chemical or physical changes in complex and opaque environments represents a fundamental technological aim.

While nanoscale emitters like quantum dots and lanthanide nanoparticles can achieve high quantum yields ($\phi_F > 0.1$) in the SWIR, organic chromophores have thus far displayed very low emission past 1000 nm ($\phi_F \leq 0.03$).[8–12] Nevertheless, organic emitters are biocompatible and provide a breadth of chemical functionalities that make them highly desirable for biological applications.[13] There is a clear trade-off between smaller HOMO-LUMO gaps and ϕ_F. Even among NIR/SWIR emitters, the higher ϕ_F dyes tend to be those with maximum absorption wavelength (λ_{max}) on the blue edge of the SWIR spectral window. In this manuscript, we apply experiment and theory to answer the questions: *What dictates fundamental limits on ϕ_F for narrow HOMO-LUMO gaps? Can we compare enhancement of ϕ_F due to a structural change between chromophores, independent of energy gap changes? What additional structural parameters provide a handle to overcome the current limits on ϕ_F?*

To address these questions, we must consider how the energy gap modulates the fluorescence quantum yield, or the ratio of the radiative rate (k_r) to the sum of radiative rate and nonradiative rate (k_{nr}),

$$\phi_F = \frac{k_r}{k_r + k_{nr}}. \quad (1)$$

Known energy gap laws modulate the radiative/non-radiative rate, which, when combined with Equation 1, allow us to derive an estimate of the maximum ϕ_F as a function of singlet energy gap (E_g) for any chromophore. This Energy gap law Quantum yield Master Equation (EQME) will allow us to frame changes in ϕ_F in terms of E_g *independent* parameters, such as the transition dipole moment (μ_{21}), Stokes shift, and the strength of nonadiabatic coupling between excited and ground states.

To parametrize and assess EQME, we utilize absorption cross sections, fluorescent spectra, excited state decay rates and quantum yields for 21 related symmetric polymethine fluorophores with absorption maxima ranging from 800–1100 nm (Figure 1).[14,15] This unique data set was acquired using sensitive superconducting nanowire single photon detectors (SNSPDs) which are capable of probing the often short excited state lifetimes of these chromophores in the SWIR, beyond the bandgap of silicon avalanche photodiodes (details in supporting information).[15–17] Comparing our results to the quantum yield of an additional 33 reported NIR and SWIR polymethine dyes demonstrates the general applicability of EQME for determining maximum quantum yield for organic chromophores in the SWIR.

The EQME equation also allows us to develop an energy gap independent comparison methodology for SWIR chromophores, enabling practical quantitative exploration how changes within a dye scaffold can lead to improved Φ_F independent of shifts in energy. Using this method, we show electron donating groups increase relative quantum yield while red-shifting the λ_{max} for the flavylium polymethine scaffold, a relationship previously obscured due to redshifting energy gaps. Furthermore, EQME quantifies other avenues for increasing quantum yield, such as deuteration, increasing the transition dipole moment through J-aggregation, or increasing the

radiative rate through plasmonic coupling. We experimentally demonstrate such improvement through partial deuteration of the Flav7 (chromophore **3**) scaffold. Our results define a metric and roadmap for overcoming limitations in SWIR quantum yields.

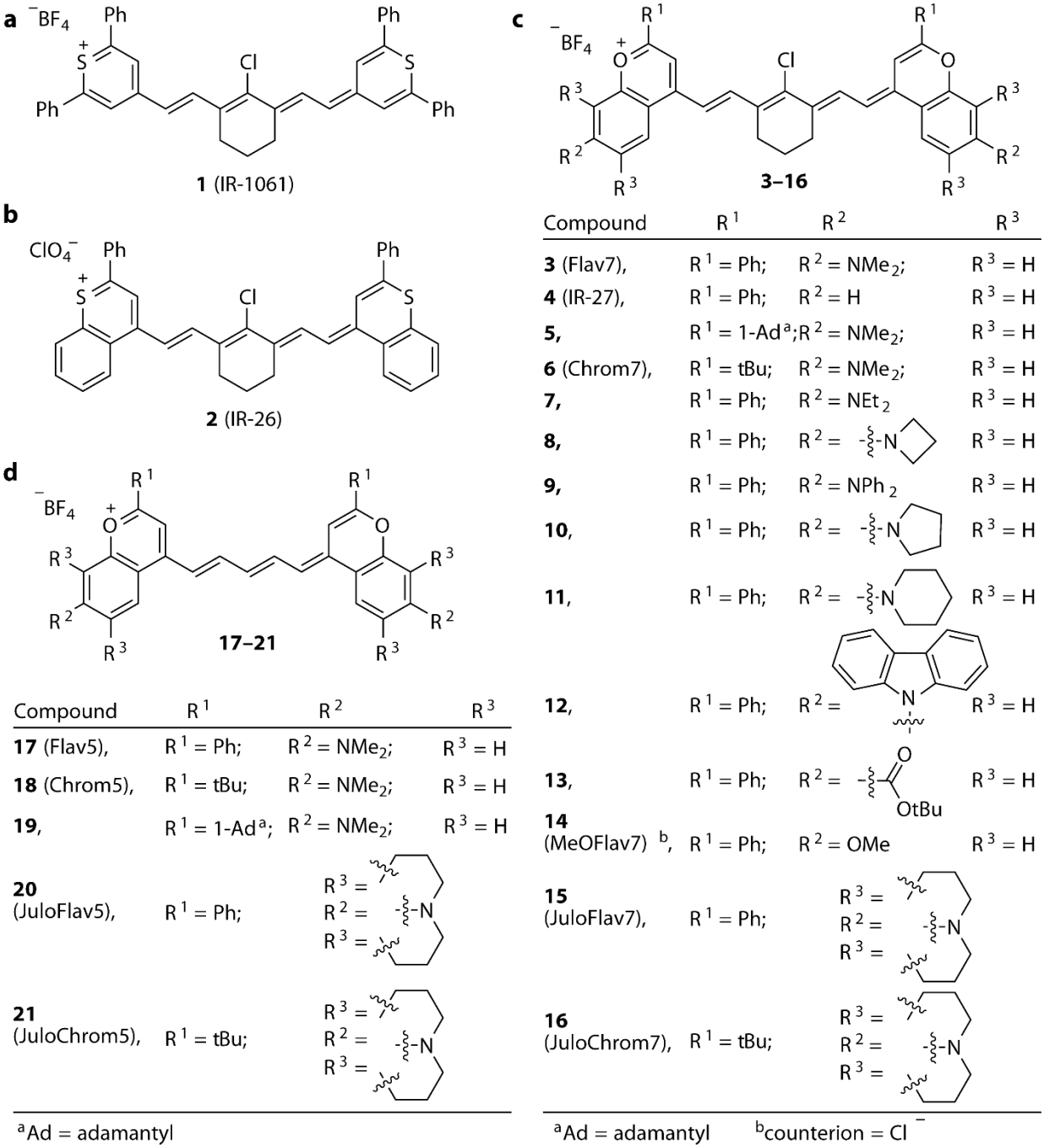

Compound	R^1	R^2	R^3
3 (Flav7),	R^1 = Ph;	R^2 = NMe_2;	R^3 = H
4 (IR-27),	R^1 = Ph;	R^2 = H	R^3 = H
5,	R^1 = 1-Ad[a];	R^2 = NMe_2;	R^3 = H
6 (Chrom7),	R^1 = tBu;	R^2 = NMe_2;	R^3 = H
7,	R^1 = Ph;	R^2 = NEt_2	R^3 = H
8,	R^1 = Ph;	R^2 =	R^3 = H
9,	R^1 = Ph;	R^2 = NPh_2	R^3 = H
10,	R^1 = Ph;	R^2 =	R^3 = H
11,	R^1 = Ph;	R^2 =	R^3 = H
12,	R^1 = Ph;	R^2 =	R^3 = H
13,	R^1 = Ph;	R^2 =	R^3 = H
14 (MeOFlav7) [b],	R^1 = Ph;	R^2 = OMe	R^3 = H
15 (JuloFlav7),	R^1 = Ph;	R^2, R^3 =	
16 (JuloChrom7),	R^1 = tBu;	R^2, R^3 =	

Compound	R^1	R^2, R^3
17 (Flav5),	R^1 = Ph;	R^2 = NMe_2; R^3 = H
18 (Chrom5),	R^1 = tBu;	R^2 = NMe_2; R^3 = H
19,	R^1 = 1-Ad[a];	R^2 = NMe_2; R^3 = H
20 (JuloFlav5),	R^1 = Ph;	R^2, R^3 =
21 (JuloChrom5),	R^1 = tBu;	R^2, R^3 =

[a]Ad = adamantyl

[a]Ad = adamantyl [b]counterion = Cl^-

Figure 1: **Chromophores studied in this manuscript.** (a/b) Laser dyes IR-1061 (a) and IR-26 (b). (c/d) Flavylium and chromenylium heptamethine (c) and pentamethine (d) fluorophores.

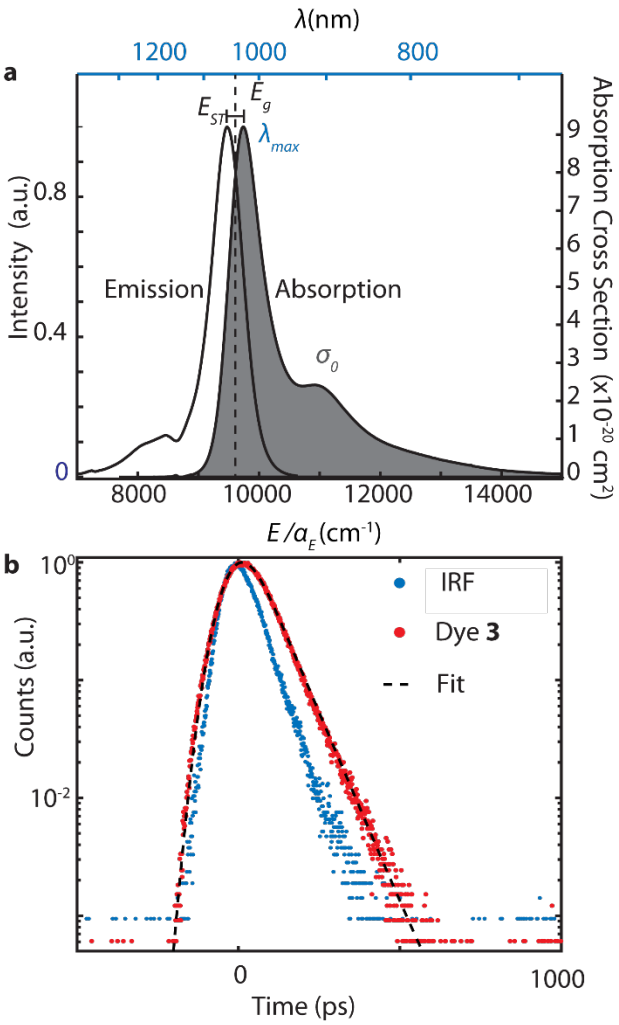

Figure 2: **Representative plots of photophysical measurements used to determine energy law constants.** a) Absorption and emission spectra for dye **3** (Flav7) in dichloromethane is plotted. λ_{max} is defined as the maximum absorption point, the E_{ST} is defined as the difference between absorption and emission maxima and σ_0 is the integrated absorption cross section. E_g is the midpoint between maximum absorption and emission values. b) Fluorescent lifetime measurement for **3**, instrument response function (IRF), and the data fit curve.

Results: In Figure 2, we show an example of the collected data used to define measured values and errors for quantum yield (ϕ_F), λ_{max}, energy gap (E_g), total rate (k_{tot}), and Stokes shift (E_{ST}). All values are reported, which were taken in DCM, in Table 1 and their measurement and fitting is detailed in Section I of the supporting information. For all derived values, we will use SI units, however the tables will report values in more conventional wavenumber units ($\tilde{\nu}$). For convenience, the values in Table 1 can be used in each equation by converting to Joules (*e.g.* multiplying by $\alpha_E = 10^2 hc \frac{\text{J}}{\text{cm}^{-1}} = 1.986 \times 10^{-23} \frac{\text{J}}{\text{cm}^{-1}}$,. E_g is defined as $\frac{hc}{\lambda_{max}} - \frac{1}{2} E_{ST}$ (Figure 2a). From the values in Table 1, we calculate the radiative and nonradiative rates (k_r and k_{nr} respectively), oscillator strengths of absorption and emission (f_{12} and f_{21}), and the excited to ground transition dipole moment (μ_{21}, μ'_{21})—calculated from the emission lifetime and absorption cross section, respectively (Table 2). The procedure for calculating these parameters is described in the Section II of the supporting information.

Table 1: Experimentally Derived Values for the Energy Gap Laws						
Dye	$\Phi_F(\times 10^{-2})$	$\frac{E_g}{\alpha_E}$ (cm^{-1})	λ_{max} (nm)	k_{tot} ($\times 10^8\ \mathrm{s}^{-1}$)	σ_0 ($\times 10^{-39}\ \mathrm{m}^2\mathrm{J}$)	$\frac{E_{ST}}{\alpha_E}$ (cm^{-1})
1	0.32 ± 0.01	9276	1063	147 ± 2	3.25 ± 0.03	258.2
2	$0.05 \pm .03$	9107	1080	490 ± 20	2.35 ± 0.04	298.7
3	0.61 ± 0.02	9603	1027	147 ± 2	2.68 ± 0.01	267.7
4	0.35 ± 0.01	10011	987	192 ± 4	2.37 ± 0.04	240.5
5	1.61 ± 0.02	10148	975	66.2 ± 0.4	2.63 ± 0.05	216.3
6	1.70 ± 0.04	10128	977	68.6 ± 0.5	2.58 ± 0.03	215.4
7	0.62 ± 0.02	9560	1033	144 ± 2	2.07 ± 0.07	237.7
8	0.51 ± 0.02	9585	1029	160 ± 3	2.86 ± 0.05	266.37
9	0.58 ± 0.02	9414	1047	147 ± 2	2.76 ± 0.01	274.7
10	0.48 ± 0.02	9548	1034	151 ± 2	2.91 ± 0.01	246.1
11	0.54 ± 0.01	9571	1030	151 ± 2	2.48 ± 0.09	274.8
12	0.45 ± 0.01	9668	1021	161 ± 3	1.46 ± 0.08	252.3
13	0.42 ± 0.02	9902	998	169 ± 3	1.16 ± 0.02	235.3
14	0.52 ± 0.01	10042	984	155 ± 2	2.03 ± 0.03	242.0
15	0.46 ± 0.01	9308	1061	180 ± 3	2.59 ± 0.02	233.9
16	1.58 ± 0.02	9814	1007	84.7 ± 0.7	2.51 ± 0.05	240.1
17	6.1 ± 0.1	11468	862	32.2 ± 0.1	3.20 ± 0.04	276.9
18	28 ± 2	12086	819	9.79 ± 0.01	3.46 ± 0.05	248.3
19	28.3 ± 0.5	12077	819	9.49 ± 0.01	2.83 ± 0.05	262.6
20	5.3 ± 0.02	10980	897	33.8 ± 0.1	2.66 ± 0.03	337.5
21	18.3 ± 0.4	11602	852	13 ± 0.1	3.67 ± 0.03	269.2
3'	0.63 ± 0.03	9626	1027	141 ± 2	4.35 ± 0.07	240.5
3"	0.66 ± 0.05	9626	1027	139 ± 2	4.40 ± 0.12	240.5

Table 2: Calculated Values for Dyes Studied						
Dye	k_r (eq 1) ($\times 10^7 s^{-1}$)	k_{nr} (eq 1) ($\times 10^8 s^{-1}$)	f_{12}	f_{21}	μ'_{21} (eq **4**) (D)*	μ_{21} (eq **3**) (D)
1	$4.7 + 0.2$	147 ± 5	4.18 ± 0.04	-0.58 ± 0.02	18 ± 3	11.5 ± 0.2
2	2.4 ± 1.4	476 ± 286	3.02 ± 0.05	-0.30 ± 0.18	15 ± 3	8.4 ± 3.0
3	$9.0 \pm .03$	146 ± 5	3.44 ± 0.01	-1.02 ± 0.04	16 ± 3	15.0 ± 0.3
4	6.7 ± 0.2	192 ± 7	3.05 ± 0.05	-0.71 ± 0.02	15 ± 2	12.3 ± 0.3
5	10.6 ± 0.3	67 ± 2	3.38 ± 0.06	-1.14 ± 0.01	15 ± 3	15.4 ± 0.1
6	11.6 ± 0.3	65 ± 1	3.31 ± 0.04	-1.16 ± 0.03	15 ± 3	15.6 ± 0.2
967	9.0 ± 0.3	144 ± 5	2.66 ± 0.10	-1.04 ± 0.04	14 ± 2	15.2 ± 0.1
8	8.2 ± 0.2	160 ± 7	3.33 ± 0.02	-0.95 ± 0.04	16 ± 3	14.5 ± 0.4
9	8.5 ± 0.3	146 ± 5	3.18 ± 0.11	-1.02 ± 0.04	15 ± 3	15.2 ± 0.3
10	7.3 ± 0.3	151 ± 7	3.54 ± 0.01	-0.84 ± 0.04	16 ± 3	13.7 ± 0.4
11	8.2 ± 0.2	151 ± 4	3.75 ± 0.02	-0.94 ± 0.02	17 ± 3	14.5 ± 0.2
12	7.3 ± 0.2	161 ± 4	1.87 ± 0.10	-0.82 ± 0.02	12 ± 2	13.4 ± 0.2
13	7.2 ± 0.4	172 ± 9	1.49 ± 0.04	-0.78 ± 0.04	10 ± 2	12.9 ± 0.4
14	8.1 ± 0.2	155 ± 4	2.61 ± 0.02	-0.85 ± 0.02	14 ± 2	13.4 ± 0.2
15	8.2 ± 0.3	178 ± 5	3.67 ± 0.07	-1.00 ± 0.03	17 ± 3	15.2 ± 0.4
16	13.4 ± 0.6	83.4 ± 4	3.22 ± 0.06	-1.47 ± 0.08	15 ± 3	17.8 ± 0.5
17	19.7 ± 0.8	30 ± 1	4.11 ± 0.05	-1.66 ± 0.03	20 ± 6	17.5 ± 0.2
18	27.4 ± 0.5	7.0 ± 0.3	4.45 ± 0.06	-2.03 ± 0.14	20 ± 5	18.9 ± 0.8
19	26.8 ± 0.4	6.8 ± 0.1	3.63 ± 0.07	-1.95 ± 0.02	18 ± 4	18.5 ± 0.2
20	18.0 ± 0.8	32 ± 1	3.41 ± 0.11	-1.49 ± 0.01	18 ± 5	17.0 ± 0.1
21	24.3 ± 0.5	10.8 ± 0.02	4.72 ± 0.04	-1.91 ± 0.04	21 ± 5	18.7 ± 0.2
3'	8.9 ± 0.5	140 ± 2	3.52 ± 0.06	-1.02 ± 0.06	16 ± 3	15.0 ± 0.4
3''	9.2 ± 0.7	138 ± 2	3.55 ± 0.09	-1.06 ± 0.08	16 ± 3	15.3 ± 0.6
***For 1–16 (17–21), $g_2/g_1 = 3 \pm 1$ (2 ± 1)**						

The First Energy Gap Law – Radiative Rates: The first law relates k_r to the density of photonic modes in vacuum (details in Section II of supporting information). Briefly, Fermi's golden rule leads to a spontaneous emission rate:

$$k_r = \frac{2\pi}{\hbar}|M_{21}|^2 g(E_g), \qquad (2)$$

where M_{21} is the transition integral and $g(E_g)$ is the density of photon states that bridge the transition energy between ground and excited states. In general, as one increases the energy gap, the density of photonic modes increases with $g(E_g) \propto {E_g}^2$ while the matrix element that couples a dipole allowed transition between excited and ground state increases with $|M_{21}|^2 \propto E_g$, leading

to a k_r which is proportional to ${E_g}^3$. For dipole allowed transitions in a solvent, the precise relationship in SI units is:

$$k_r = \frac{n\mu_{21}^2}{3\pi\epsilon_0\hbar^4c^3}E_g^3, \tag{3}$$

where ϵ_0 is the vacuum permittivity, and n is the refractive index of the solvent ($n = 1.42$ for dichloromethane).

To assess the validity of the radiative rate energy gap law across different chromophores, we must normalize each rate by the molecule's squared transition dipole moment (μ_{21}^2) as assessed by a *separate measurement*, in this case the integrated absorption cross section:[18]

$$|\mu_{21}'|^2 = 3\frac{g_1\epsilon_0 n\hbar c}{g_2\pi E_g}\sigma_0. \tag{4}$$

where, $g_2/g_1$is the ratio of oscillator strength of polymethines of absorption and emission, respectively, or $-f_{12}/f_{21}$. We note that in polymethine chromophores, the absorption oscillator strength depends on the length of the methine bridge. For cyanine dyes with 7 methine units, prior reports show values between 2–3 and with shorter methine bridges values between 1.7–1.9 are reported. [19–21] We therefore use the average values $g_2/g_1 = 3 \pm 1$ for 7-methines (**1**–**16)** and 2 ± 1 for 5-methines (**17**–**21)**.* In Figure 3, we plot the radiative rate divided by the transition dipole moment, and compare to the following universal gap law:

$$\frac{k_r}{\mu_{21}^2} = K_\mu\frac{n}{3\pi\epsilon_0\hbar^4c^3}E_g^3. \tag{5}$$

* We note the two primary outliers are **1** and **2** (commercially known as IR-1061 and IR-26). Both dyes have thiochromenylium derived heterocycles. Our results suggest that the presence of sulfur on the heterocycle leads to large deviations in the oscillator strength ratio from changes in f_{21}.

Here, $K_\mu = 1.11 \times 10^{-59} \mathrm{C^2 m^2 D^{-2}}$ (a conversion factor which allows us to express μ_{21} in more convenient Debye units). We observe that the transition dipole moment normalized radiative rate follows an approximate E_g^3 power law. This is consistent with the change in the density of states as a function of gap.

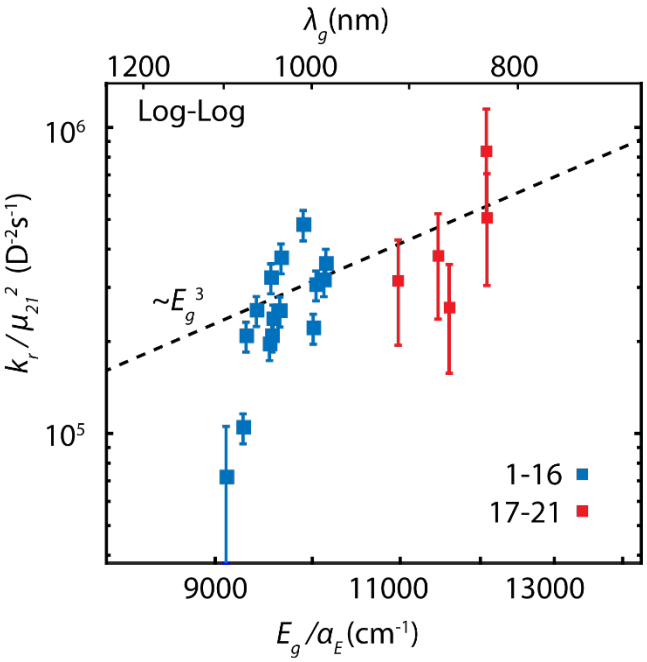

Figure 3**: Polymethines follow the radiative rate energy gap law.** Radiative rates from Table 2 divided by transition dipole moment from Equation 4 for heptamethines (blue) and pentamethines (red). Line represents Equation 5 , the radiative rate gap law normalized to transition dipole moment, allowing us to compare the dyes independent of the specific molecular parameters.

The Second Energy Gap Law – Nonradiative Rates: Nonradiative rates are governed by multiple excited state loss channels including internal conversion (decay through vibrational modes), intersystem crossing (decay through an intermediate triplet state), and nuclear reorganization (decay to a lower energy molecular configuration, for example through isomerization or proton transfer).[22–24] The *second energy gap law* states that nonradiative relaxation rates for intersystem crossing and internal conversion (k_{nr}) exponentially decrease at higher E_g. Here, we focus on singlet states and thus nonradiative decay through internal conversion, allowing us to establish a lower bound on k_{nr} for infrared chromophores.

The experimental values for nonradiative rates are compared to the expression derived by Englman and Jortner,[24] which provides the nonradiative gap law in systems that have small Stokes shifts (E_{ST}) relative to their energy gap, E_g. We present a modified expression below (derived in the supporting information Section III) which relates this equation to values found in Table 1:

$$k_{nr} = \frac{C^2\sqrt{2\pi}}{\hbar\sqrt{E_M E_g}} \exp\left[-\frac{E_g}{E_M}\left(\ln\left(\frac{2E_g}{\gamma_M E_{ST}}\right) - 1\right)\right]. \quad (6)$$

Here, C is the non-adiabatic coupling term between singlet ground and excited states and E_M is the energy of the deactivating vibrational mode. γ_M is a parameter representing the degree to which the deactivating mode contributes to the Stokes shift given by:

$$\gamma_M = \frac{SE_M}{E_{ST}}, \quad (7)$$

where S is the Huang-Rhys parameter for the collection of near degenerate vibrational modes at or near E_M. Over the range of energies considered, the nonradiative rate will exponentially decrease with increasing energy gap, as observed in many systems, including gold nanoclusters,[25] metal to ligand charge transfer complexes,[26,27] aromatic thiones,[28] and platinum containing conjugated polymers.[29]

To predict the energy gap dependence of nonradiative rates for polymethine chromophores studied here, we require semi-empirical estimates of E_M, γ_M, and C. For all estimates, we will use the largest Stokes shift for 7-methine dyes in Table 1 (dye **2**, $E_{ST} = 298.7\ \mathrm{cm}^{-1}$). E_M is the energy of the vibration which contributes most strongly to the overlap between ground and excited states. While a more detailed derivation is provided in reference 24, conceptually the gap law arises from the overlap between ground and excited state potentials, which varies nonlinearly with the vibrational energy. If the energy gap and Stokes shift are fixed, the tunneling distance between potentials decreases with the vibrational curvature (energy) of the mode. In the limit of large E_g relative to E_{ST}, higher energy vibrations dominate contributions to the overlap integral between ground and excited states. As in reference 21, we will use $E_M = 3000\ \mathrm{cm}^{-1}$ for Equation 7, the approximate energy of the collection of C-H vibrational modes.

We will use pessimistic estimates for γ_M and C to provide a worst-case scenario for the energy gap law for nonradiative rates. Hence, we estimate $\gamma_M = 1$, meaning the singular contributor to the Stokes shift are the C-H vibrational modes. We note that this results in a collective Huang-Rhys parameter of $S = 0.1$ for all combined C-H stretches (Equation 7), leading to a relatively small vibronic progression in a calculated absorption spectrum (Figure S3). To estimate the derivative non-adiabatic coupling, C, we assert that all experimental nonradiative rates are either equal or larger than predicted by Equation 6 and use the largest Stokes shift in the 7-methine dye data set, (dye **2**, $E_{ST} = 298.7\ \mathrm{cm}^{-1}$), to arrive at the minimum possible value of C, corresponding to chromophore **1** ($C = 4080\ \mathrm{cm}^{-1}$). Again, this gives us a pessimistic estimate for the nonadiabatic coupling parameter that is still consistent with our data (Figure 4).

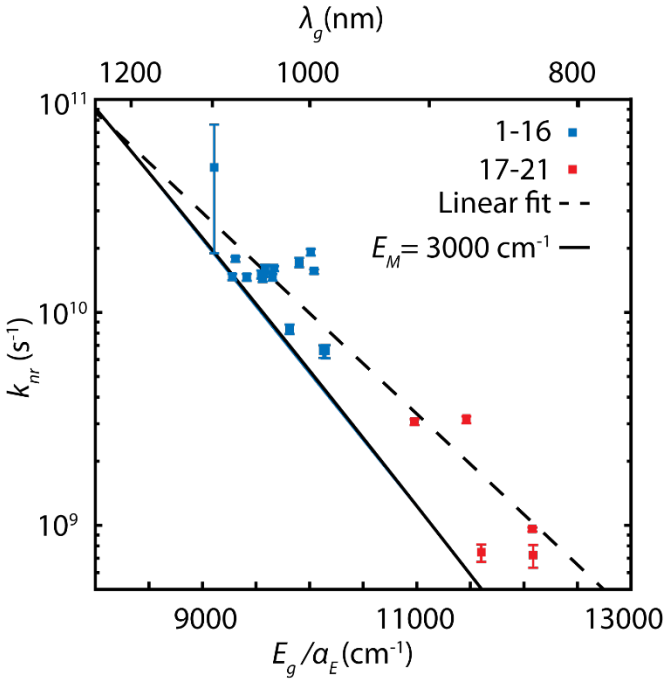

Figure 4: **k_{nr} are governed by high frequency vibrational modes $E_M > 3000\ cm^{-1}$**. Nonradiative rates from Table 2 plotted against linear fit of $log\ (k_{nr})$, and Equation 6, evaluated using the parameters described in the text.

In order to reinforce the assumption that the highest frequency vibrational mode would dominate the nonradiative rate, we note the linear change in $\log(k_{nr})$ as a function of energy gap in Figure 4. Despite a large variance in quantum yield among these dyes, this linear trend strongly implies that energy gap law considerations dominate the nonradiative relaxation rates in the SWIR. We plot the nonradiative rate estimate from Equation 6 using the parameters described in the preceding section ($E_{ST} = 298.7\ \mathrm{cm}^{-1}, C = 4080\ \mathrm{cm}^{-1}$), which shows good agreement with the

nonradiative rate data. We also perform a linear fit of the data from which we extract the slope, which corresponds to

$$\frac{d\log(k_{nr})}{dE_g} = -\log(e)\left(\frac{1}{2E_g'} - \frac{\ln\left(\frac{2E_g'}{\gamma_M E_{ST}}\right)}{E_M}\right) \tag{8}$$

For simplicity, we will use the midpoint $E_g' = 10{,}000\ \mathrm{cm}^{-1}$, which leads to a fit for the deactivating vibrational mode of $E_M^{fit} = 4086\ \mathrm{cm}^{-1}$. Taken together, both the agreement of the model and the slope from the linear fit agree with the apparent dominance of *high-frequency vibrational* modes ($\geq 3000\ \mathrm{cm}^{-1}$, i.e. C-H stretches) in setting the non-radiative rate limit in SWIR-emitting polymethines.

Energy Gap Quantum Yield Master Equation: We can combine Equations 1, 3 and 6 to derive EQME, which sets the maximum quantum yield of as function of energy gap, dielectric and molecular parameters:

$$\phi_F(E_g) = \left(1 + K\frac{C^2}{n\mu_{21}^2\left(E_M E_g^7\right)^{\frac{1}{2}}}\exp\left[-\frac{E_g}{E_M}\left(\ln\frac{2E_g}{\gamma_M E_{ST}} - 1\right)\right]\right)^{-1}, \tag{9}$$

where $K = \left(\frac{3\epsilon_0 c^2}{(2^5\pi^3)^{1/2}}\right)$. In Figure 5, we plot the functional form of the predicted "highest" quantum yield using $\gamma_M = 1$, $C_p = 4080\ \mathrm{cm}^{-1}$, $\mu_{21} = 18$ D and $E_{ST} = 298.7\ \mathrm{cm}^{-1}$. We also include a

more optimistic limit, $C_O = 2000\ \mathrm{cm}^{-1}$, which approximates a median value for the derivative coupling from literature on polyacenes and polyenes.[30,31] A smaller coupling to the high frequency stretches ($\gamma_M = 0.5$) (Figure S4 shows effects of changes C and γ_M independently). We plot both our measured quantum yields from this work and 32 additional dyes from literature reports (see Figure S5 for labeled points).[4,13–15,32–38] Our results demonstrate that even under pessimistic assumptions, quantum yields of almost all observed polymethine dyes do not exceed our predicted maximum line, with an exception of the LZ series of dyes reported by Li *et al.*[12,39] Given that our pessimistic estimation likely over-estimates the impact of nonadiabatic coupling, a few outliers can be expected. What is clear is that the model demonstrates that the precipitous falloff in quantum yields around 900 nm is an unavoidable consequence of energy gap laws applied to organic chromophores.

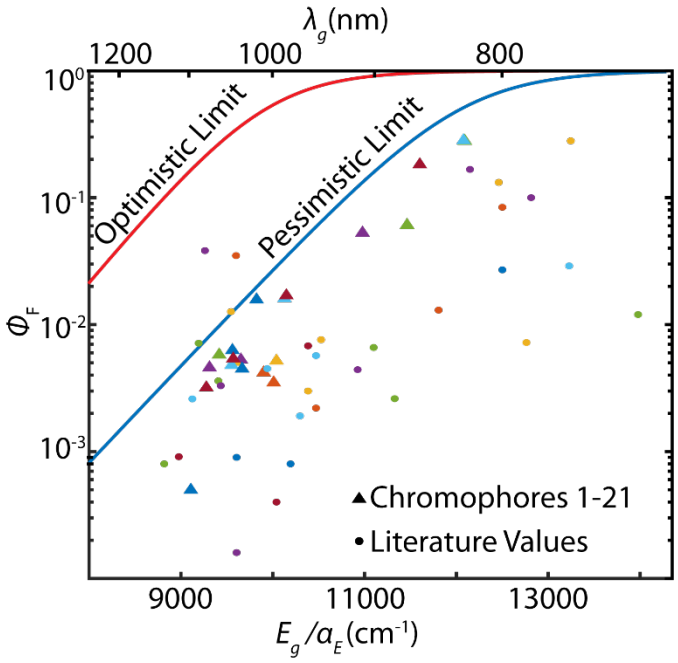

Figure 5: **EQME provides consistent upper bounds for SWIR quantum yields.** Comparison of quantum yields of 54 NIR and SWIR polymethine chromophores to the prediction of EQME (Equation 9).

Comparing Chromophore Quantum Yield while Accounting for Energy Gap Changes: It is challenging to predict how structural modifications of a chromophore will alter the quantum yield. We hypothesize that the dearth of predictive metrics (particularly in the SWIR) arises from the contribution of energy gap QY changes which disguise the underlying effects of molecular change. Using EQME, we can establish an *energy-gap independent* parameter (ξ) to study the effect of structural changes on quantum yields within a chromophore family.

We first define a conventional improvement factor (χ) as the fractional change in quantum yield, e.g. $\chi = \phi_b/\phi_a - 1$ ($\chi > 0$ indicates a direct improvement in ϕ_F). To create an energy gap independent metric, we first note that when $k_{nr} \gg k_r$ (e.g., when $\phi_F < 0.1$), $\log(\phi_F)$ is approximately linear with respect to E_g changes. We therefore can extrapolate Φ_F of a chromophore at one E_g to its equivalent value at another point in the SWIR. Comparing the extrapolated quantum yield of the standard fluorophore (**a**) to a second fluorophore (**b**) at the E_g of **b** gives us an energy-gap independent improvement factor, ξ.

$$\xi = \frac{\phi_b}{\phi_a} e^{-\kappa(E_b - E_a)} - 1 \tag{10}$$

Where κ is

$$\kappa = \frac{\ln\left(2E_{g,a}/\gamma_M E_{ST,a}\right)}{E_M} + \frac{7}{2E_{g,a}} \tag{11}$$

$\xi > 0$ indicates an improvement in the quantum yield factoring in the effect of changing the energy gap. The differences between χ and ξ are illustrated in Figure 6a; Equation 11 is derived in section V of the supporting information, with Figure S6 showing the validity of our assumptions for κ, and Figure S7 showing a worked example using ξ.

Having established a comparative metric for SWIR fluorophore quantum yield that is independent of energy gap we compare across heptamethine fluorophores with systematic changes at the 7-position of the flavylium ring (dyes **3, 4**, **7**–**11, 13**–**15**). Using Equation 10, we computed

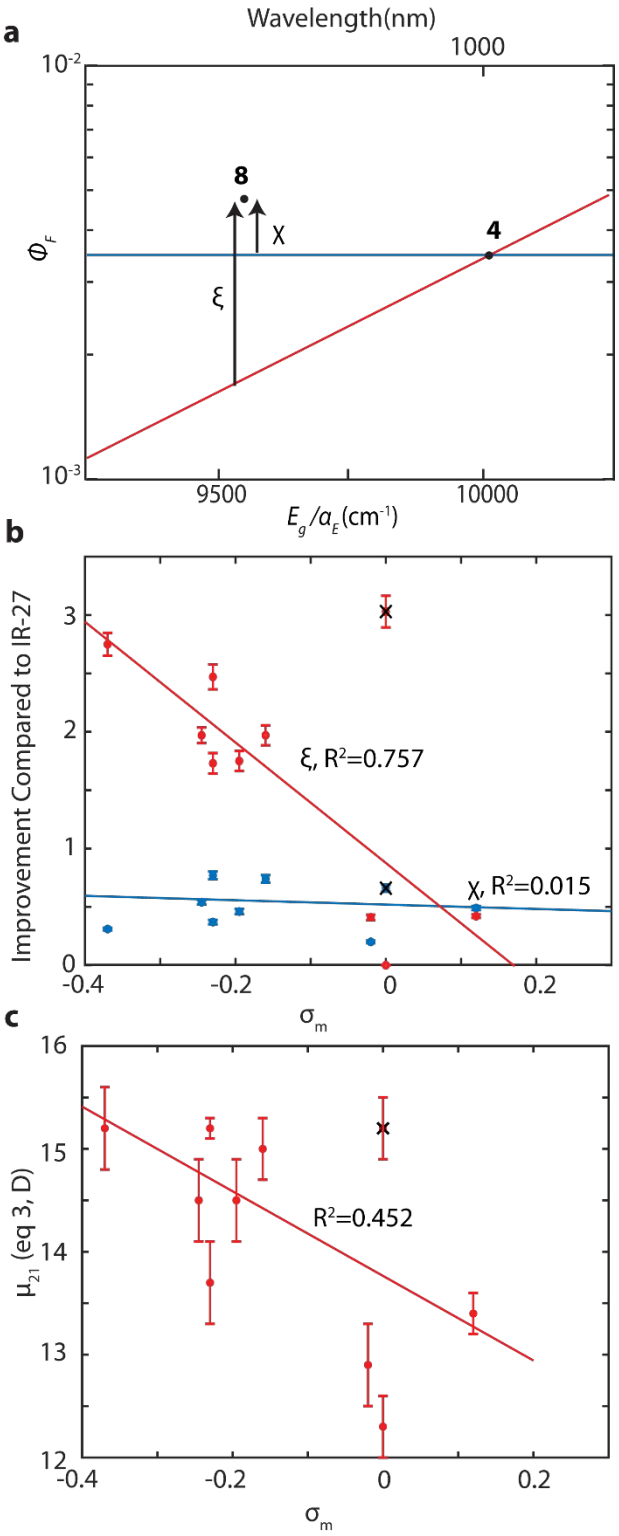

Figure 6: **Energy gap free QY comparator, ξ uncovers a linear free energy relationship.** a) Example of the difference between ξ *and* χ b) ξ shows correlation with Hammett parameter while chi shows negligible correlation. X through points denotes dye **9** which is excluded from all fits as done in ref. 14. c) There is a negative correlation between Hammett parameter σ_m and transition dipole moment.

ξ values using the unsubstituted IR-27 (**4**) as the comparative fluorophore (*i.e.* fluorophore **a**). These values are in Table 3 (Figure S8 for all values plotted like in Figure 6a). The ξ parameter reveals large energy gap independent changes in quantum yield hidden in the direct improvement factor. For example, chromophore **15** displays 2.75 ξ improvement despite a more modest χ improvement of 0.31.

Using ξ we sought to correlate the energy gap independent improvement factor with the Hammett σ_m parameter.[40] Prior work demonstrated that the absorption and emission maximum correlated well to σ_m ($R^2 = 0.96$); however, the quantum yield showed no direct correlation.[14] In Figure 6b, we show no correlation between σ_m and χ (blue line, $R^2 = 0.015$). However, when ξ is plotted against σ_m values, a linear correlation emerges (Figure 6b, red line $R^2 = 0.757$). Our results suggest that electron donation enhances the quantum yield. In

Table 3: Enhancement of Dyes Compared to Dye 4 (IR-27)		
Dye	ξ	χ
1	1.73	−0.09
2	−0.45	−0.86
3*	1.97	0.74
5	2.75	3.60
6	3.08	3.86
7*	2.47	0.77
8*	1.75	0.46
9*	3.03	0.66
10*	1.73	0.37
11*	1.97	0.54
12	1.14	0.29
13*	0.41	0.20
14*	0.42	0.49
15*	2.75	0.31
16	5.05	3.51
***included in Hammett parameter analysis**		

Figure 6c, we show that transition dipole moment, μ_{21}, also increases with decreasing σ_m (R^2 = 0.452). We therefore hypothesize that electron donating groups appended to the heterocycle functionally increase the delocalization length of the excitation, leading to redshifting chromophores and larger transition dipole moments. Increased μ_{21} partially compensates for the reduction in quantum yield due to the redshift.

Overcoming energy gap laws: The EQME suggests pathways to directly improve the quantum yield of organic chromophores through changes in radiative and nonradiative rates (Figure 7a). To alter the radiative rate of the chromophore, one can either A) alter the transition dipole moment, μ_{12}, or B) control the local photon density of states ($g(E_g)$). For (A), a potential approach is molecular J-aggregation in which coupled chromophores collectively interact with an electric field, resulting in superradiant emission.[41]. Furthermore, J-aggregation has the advantage of both modulating the radiative rate and redshifting the absorption and emission. Indeed, several groups have had success in using this strategy to access highly redshifted organic chromophores though superradiance has not been shown.[42,43] Chen *et al.* showed that J-aggregation of IR-140 shifted λ_{max} from 803 nm in DCM to 1042 nm in 35% DMSO, 0.9% water solution and changed its ϕ_F from $17\ to\ 0.01 \times 10^{-2}$.[33,42] Sun *et al.* demonstrated that FD-1080 J-aggregates into nanoparticles ligated with phospholipid which have a λ_{max} of 1370 nm and a quantum yield of 5.45×10^{-4} compared to the monomer values of 1046

nm and $\phi_F = 3.1 \times 10^{-3}$ in ethanol.[35,43]. For (B), the most common path discussed is through incorporation of photonic cavities or coupling to plasmonic nanoparticles.[44–46] Historically, microdroplets have been shown to modulate the radiative rate; for example, Rhodamine-6G showed an improvement of 2 in smaller droplet compared to larger droplets, including a change in fluorescence rate.[44,45] Srinivasan and Ramamurthy showed that Rhodamine-6G in cermet nanocavities had greater than 50-fold fluorescence enhancement. Lu *et al.* demonstrated that a NIR emitting molecule based on naphthalene diimide-terthiophene ($\lambda_{max} = 590$ nm, $E_{st} = 3000\ cm^{-1}$ and $\phi_F = 1.3 \times 10^{-4}$) near a gold nanorod whose plasmon is at 673 nm, shows an enhancement factor of about 6500.[46] Though these pathways are promising, the impact of plasmonic/photonic modifications on the nonradiative rates needs to be studied in more detail.[47–49]

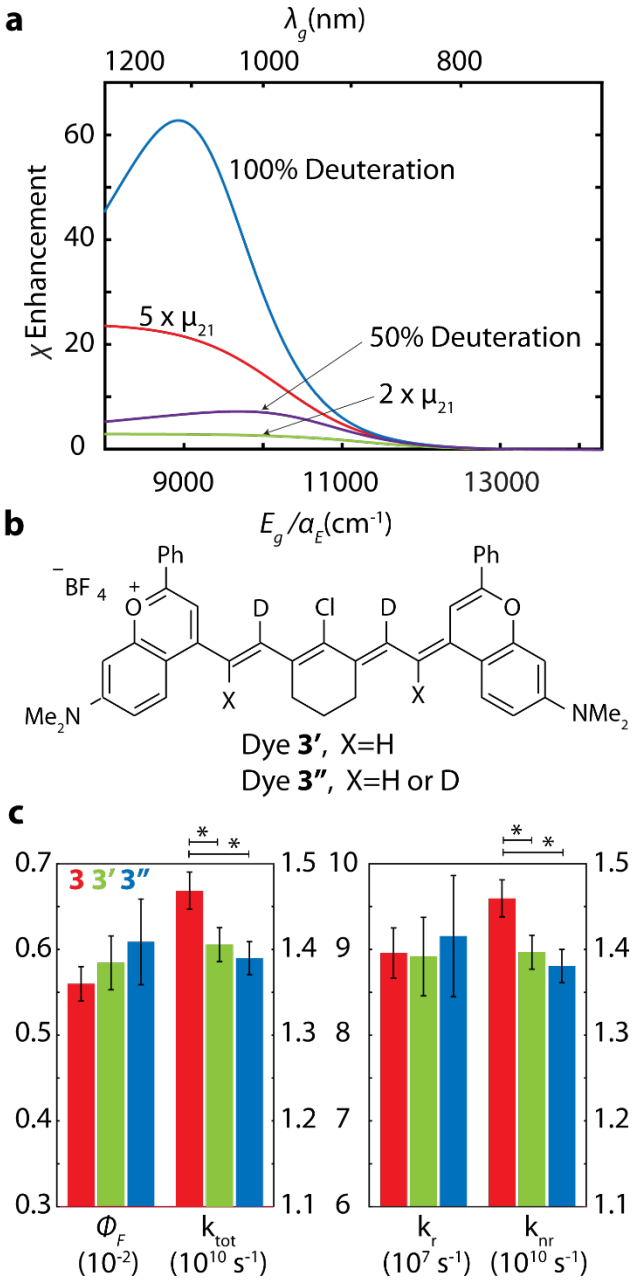

Figure 7: **Deuteration and increased transition dipole moment enhances PLQY in SWIR**. a) Ratiometric enhancement in quantum yield as a function of energy gap for different strategies for circumventing the energy gap laws including complete deuteration of the alkenyl CH stretches (blue), 50 percent deuteration (purple), increasing the transition dipole moment by 5 and 2 (red and yellow). b) Structures of dye **3'** and **3"**. c) deuteration on the polymethine scaffold increases but not significantly quantum yield, decreases total rate, has negligible effect on radiative rate, and decreases nonradiative rate. The asterisk indicates that the difference between dyes is significant $p < 0.05$.

For nonradiative rates, the highest vibrational frequency plays a large role in setting k_{nr}, typically the alkenyl C-H stretch at 3000 cm^{-1}. Complete substitution of H for D would change the highest vibrational energy to 2200 cm^{-1}. Assuming no change in the Huang-Rhys parameter (S) we predict a maximum ~60 fold enhancement in quantum yield, using the pessimistic assumptions (Figure 7a, ~40 under optimistic assumptions (Figure S9). Prior work on Iridium complexes,[50] benzene,[51] oxazine,[52] and small molecule for blue LEDs[53] also demonstrated increased quantum yields with deuteration suggesting deactivation through these modes is a common feature in chromophores.

To test the effect of deuteration on polymethine chromophores, we synthesized two partially deuterated Flav7 (**3**), derivatives, **3'** and **3"** (structures in Figure 7b). We hypothesized that partial deuteration will only have a modest effect on the

nonradiative rate by decreasing the collective Huang-Rhys parameter of the highest energy mode. Measuring absorption, quantum yield, and time resolved photoluminescence lifetime (section S1) we observe that dyes **3'** and **3"** display a slight quantum yield enhancement ($\chi = 0.04 \pm 0.04$ and 0.08 ± 0.08, respectively), despite near identical absorption and emission spectra (Figure S10). While the quantum yield and radiative rate changes are within the error of the measurement, the change in k_{tot} and k_{nr} are significant ($p<0.05$ for both compared to dye **3**, Figure 7c, and details in section S5). The change in k_{tot} and k_{nr} between dye **3'** and **3"** are not significant, in part because dye **3"** is a mixture that mostly comprises **3'**, however the trend suggests that more deuteration improves these qualities (section S5).

Discussion:

Every chromophore system is subject to the same energy gap laws described above, however, our data suggests that polymethine dyes have some of the best intrinsic properties for SWIR absorption and emission, including high transition dipole moments and small Stokes shifts.[54] Even with these favorable properties, the energy gap laws strongly suggest emission quantum yields of NIR/SWIR organic fluorophores will remain around 3% or less unless fundamental changes to the radiative and non-radiative pathways are realized. It further explains why techniques used to systematically improve the quantum yield in the visible spectra (e.g. rigidification) has not led to equivalent improvements for NIR/SWIR chromophores.[20] Using the cyanine dyes as an example for the effects conformational restriction across the visible to the NIR regions, ϕ_F (λ_{max}) is 0.09 (550 nm) and 0.85 (558 nm) in water for Cy3 and Cy3B,[55–57] respectively, 0.15 (638 nm) and 0.69 (662 nm) in methanol for Cy5 and Cy5B,[58] respectively, and 0.24 (740 nm) and 0.29 (782 nm) in methanol for Cy7 and Cy7B, respectively.[20] On the other hand, for polymethines, deuteration *should not significantly improve quantum yields in the visible*

or near infrared ($\lambda_{max} < 900\,nm$), as other nonradiative pathways govern excited state dissipation in that window.

Focusing here on nonradiative decay pathways, we find that SWIR chromophores are deactivated via omnipresent vibronic coupling which directly connects ground and excited states through tunneling, mediated by C-H stretches. However, identifying precisely which C-H stretches should be modified remains an open question. Recent work by Hirata *et al.* on deuteration of N,N′-diphenyl-N,N′-(3-methyl phenyl)-1,1′-biphenyl-4,4′-diamine (TPD) reports suggests that the location of the deuteration will have differential effects on the vibronic manifold, suggesting that some stretches are privileged in dissipative dynamics.[53] Specifically, TPD has a phosphorescence quantum yield of 0.030 ± 0.003, deuteration of the exterior phenyl amine only increases the quantum yield to 0.032 ± 0.003, while deuteration of the diphenyl core increases the quantum yield to 0.062 ± 0.005 and deuteration of every hydrogen increases the quantum yield to 0.060 ± 0.005.[53] Further supporting this view, systems with high QYs in the SWIR (Pb and Hg chalcogenide nanocrystals, lanthanide f-orbital centers), have transitions which couple mostly to low-frequency phonon modes, i.e. $E_M/a_E \leq 300\ \mathrm{cm}^{-1}$,[9] consistent with higher QYs and considerably weaker direct nonradiative decay pathways

Conclusion

To make systematic improvements to SWIR chromophores, we first explore the validity of energy gap laws for radiative and nonradiative rates and apply it to analyze a large data set of NIR/SWIR polymethine dyes. We derive an energy gap quantum yield master equation which demonstrates that the precipitous drop in quantum yields in the SWIR is consistent with the exponentially increasing nonradiative decay rates and decreasing radiative rates, with the former mediated by the presence of high frequency vibrational modes. Energy gap laws must be

considered when comparing NIR/SWIR chromophores as improvements to quantum yield are directly correlated to the energy gap. By creating energy gap neutral parameters, we elucidate the impact of simple structural derivatives on quantum yield. We thus assess the natural limits of quantum yield in chromophores and provide a path forward in the inverse design problem. The presence of organic alkenyl C-H stretches likely limits the maximum possible quantum yield for SWIR emitters, but our preliminary results suggest that deuteration and judicious chromophore design may provide a path forward. We believe that a general and unified framework will enable the design of novel SWIR chromophore systems beyond the polymethine chromophore class and enable rational optimization of fluorescence in these systems.

Acknowledgments: This work was supported by NSF CHE grant no. CHE-1905242, CHE-1945572, NIBIB grant no. 1R01EB027172, and instrumentation grants NSF CHE-1048804 and NIH 1S10OD016387. HCF thanks the SG Fellowship and UCLA Graduate Council Diversity Fellowship. EDC thanks NSF GFRP DGE-1144087 and the Foote Family. JRC thanks the Research Corporation Cottrell Fellowship.

References

(1) Hong, G.; Antaris, A. L.; Dai, H. Near-Infrared Fluorophores for Biomedical Imaging. *Nat. Biomed. Eng.* **2017**, *1* (1), 0010. https://doi.org/10.1038/s41551-016-0010.

(2) Lautenschläger, G.; Gessner, R.; Gockel, W.; Haas, C.; Schweickert, G.; Bursch, S.; Welsch, M.; Sontag, H. Sentinel-2: Next Generation Satellites for Optical Land Observation from Space. In *Sensors, Systems, and Next-Generation Satellites XVII*; 2013; Vol. 8889, p 88890L. https://doi.org/10.1117/12.2028725.

(3) Carr, J. A.; Valdez, T. A.; Bruns, O. T.; Bawendi, M. G. Using the Shortwave Infrared to Image Middle Ear Pathologies. *Proc. Natl. Acad. Sci. U. S. A.* **2016**, *113* (36), 9989–9994. https://doi.org/10.1073/pnas.1610529113.

(4) Cosco, E. D.; Caram, J. R.; Bruns, O. T.; Franke, D.; Day, R. A.; Farr, E. P.; Bawendi, M. G.; Sletten, E. M. Flavylium Polymethine Fluorophores for Near- and Shortwave Infrared Imaging. *Angew. Chem. Int. Ed.* **2017**, *56* (42), 13126–13129. https://doi.org/10.1002/anie.201706974.

(5) Bruns, O. T.; Bischof, T. S.; Harris, D. K.; Franke, D.; Shi, Y.; Riedemann, L.; Bartelt, A.; Jaworski, F. B.; Carr, J. A.; Rowlands, C. J.; Wilson, M. W. B.; Chen, O.; Wei, H.; Hwang, G. W.; Montana, D. M.; Coropceanu, I.; Achorn, O. B.; Kloepper, J.; Heeren, J.; So, P. T. C.; Fukumura, D.; Jensen, K. F.; Jain, R. K.; Bawendi, M. G. Next-Generation in Vivo Optical Imaging with Short-Wave Infrared Quantum Dots. *Nat. Biomed. Eng.* **2017**, *1* (4). https://doi.org/10.1038/s41551-017-0056.

(6) Carr, J. A.; Franke, D.; Caram, J. R.; Perkinson, C. F.; Saif, M.; Askoxylakis, V.; Datta, M.;

Fukumura, D.; Jain, R. K.; Bawendi, M. G.; Bruns, O. T. Shortwave Infrared Fluorescence Imaging with the Clinically Approved Near-Infrared Dye Indocyanine Green. *Proc. Natl. Acad. Sci. U. S. A.* **2018**, *115* (17), 4465–4470. https://doi.org/10.1073/pnas.1718917115.

(7) Kutila, M.; Pyykonen, P.; Holzhuter, H.; Colomb, M.; Duthon, P. Automotive LiDAR Performance Verification in Fog and Rain. In *IEEE Conference on Intelligent Transportation Systems, Proceedings, ITSC*; Institute of Electrical and Electronics Engineers Inc., 2018; Vol. 2018-November, pp 1695–1701. https://doi.org/10.1109/ITSC.2018.8569624.

(8) Wan, H.; Du, H.; Wang, F.; Dai, H. Molecular Imaging in the Second Near-Infrared Window. *Advanced Functional Materials*. 2019. https://doi.org/10.1002/adfm.201900566.

(9) Semonin, O. E.; Johnson, J. C.; Luther, J. M.; Midgett, A. G.; Nozik, A. J.; Beard, M. C. Absolute Photoluminescence Quantum Yields of IR-26 Dye, PbS, and PbSe Quantum Dots. *J. Phys. Chem. Lett.* **2010**, *1* (16), 2445–2450. https://doi.org/10.1021/jz100830r.

(10) Hatami, S.; Würth, C.; Kaiser, M.; Leubner, S.; Gabriel, S.; Bahrig, L.; Lesnyak, V.; Pauli, J.; Gaponik, N.; Eychmüller, A.; Resch-Genger, U. Absolute Photoluminescence Quantum Yields of IR26 and IR-Emissive Cd1-XHgxTe and PbS Quantum Dots-Method- and Material-Inherent Challenges. *Nanoscale* **2015**, *7* (1), 133–143. https://doi.org/10.1039/c4nr04608k.

(11) Hu, J. Y.; Ning, Y.; Meng, Y. S.; Zhang, J.; Wu, Z. Y.; Gao, S.; Zhang, J. L. Highly Near-IR Emissive Ytterbium(Iii) Complexes with Unprecedented Quantum Yields. *Chem. Sci.* **2017**, *8* (4), 2702–2709. https://doi.org/10.1039/C6SC05021B.

(12) Li, B.; Zhao, M.; Feng, L.; Dou, C.; Ding, S.; Zhou, G.; Lu, L.; Zhang, H.; Chen, F.; Li, X.; Li, G.; Zhao, S.; Jiang, C.; Wang, Y.; Zhao, D.; Cheng, Y.; Zhang, F. Organic NIR-II Molecule with Long Blood Half-Life for in Vivo Dynamic Vascular Imaging. *Nat. Commun.* **2020**, *11* (1), 3102. https://doi.org/10.1038/s41467-020-16924-z.

(13) Ding, B.; Xiao, Y.; Zhou, H.; Zhang, X.; Qu, C.; Xu, F.; Deng, Z.; Cheng, Z.; Hong, X. Polymethine Thiopyrylium Fluorophores with Absorption beyond 1000 Nm for Biological Imaging in the Second Near-Infrared Subwindow. *J. Med. Chem. 62* (4), 2049–2059. https://doi.org/10.1021/acs.jmedchem.8b01682.

(14) Cosco, E. D.; Spearman, A. L.; Ramakrishnan, S.; Lingg, J. G. P.; Saccomano, M.; Pengshung, M.; Arús, B. A.; Wong, K. C. Y.; Glasl, S.; Ntziachristos, V.; Warmer, M.; McLaughlin, R. R.; Bruns, O. T.; Sletten, E. M. Shortwave Infrared Polymethine Fluorophores Matched to Excitation Lasers Enable Non-Invasive, Multicolour in Vivo Imaging in Real Time. *Nat. Chem.* **2020**, *12* (12), 1123–1130. https://doi.org/10.1038/s41557-020-00554-5.

(15) Cosco, E. D.; Arús, B. A.; Spearman, A. L.; Atallah, T. L.; Lim, I.; Leland, O. S.; Caram, J. R.; Bischof, T. S.; Bruns, O. T.; Sletten, E. M. Bright Chromenylium Polymethine Dyes Enable Fast, Four-Color In Vivo Imaging with Shortwave Infrared Detection. *J. Am. Chem. Soc.* **2021**. https://doi.org/10.1021/jacs.0c11599.

(16) Mattioli, F.; Zhou, Z.; Gaggero, A.; Tanner, M. G.; San, L.; Alvarez, E.; Jiang, W.; Subashchandran, S.; Okamoto, R.; Zhang, L.; Engel, A.; Renema, J. J.; Il 'in, K.; Natarajan, C. M.; Tanner, M. G.; Hadfield, R. H. Superconducting Nanowire Single-Photon Detectors: Physics and Applications. *Supercond. Sci. Technol. Supercond. Sci. Technol* **2012**, *25* (25),

63001–63016. https://doi.org/10.1088/0953-2048/25/6/063001.

(17) Atallah, T. L.; Sica, A. V.; Shin, A. J.; Friedman, H. C.; Kahrobai, Y. K.; Caram, J. R. Decay-Associated Fourier Spectroscopy: Visible to Shortwave Infrared Time-Resolved Photoluminescence Spectra. *J. Phys. Chem. A* **2019**, *123* (31), 6792–6798. https://doi.org/10.1021/acs.jpca.9b04924.

(18) Hilborn, R. C. Einstein Coefficients, Cross Sections, f Values, Dipole Moments, and All That. *Am. J. Phys.* **1982**, *50* (11), 982–986. https://doi.org/10.1119/1.12937.

(19) Štacková, L.; Muchová, E.; Russo, M.; Slavíček, P.; Štacko, P.; Klán, P. Deciphering the Structure–Property Relations in Substituted Heptamethine Cyanines. *J. Org. Chem.* **2020**, *85* (15), 9776–9790. https://doi.org/10.1021/acs.joc.0c01104.

(20) Matikonda, S. S.; Hammersley, G.; Kumari, N.; Grabenhorst, L.; Glembockyte, V.; Tinnefeld, P.; Ivanic, J.; Levitus, M.; Schnermann, M. J. Impact of Cyanine Conformational Restraint in the Near-Infrared Range. *J. Org. Chem.* **2020**, *85* (9), 5907–5915. https://doi.org/10.1021/acs.joc.0c00236.

(21) Karaca, S.; Elmacı, N. A Computational Study on the Excited State Properties of a Cationic Cyanine Dye: TTBC. *Comput. Theor. Chem.* **2011**, *964* (1–3), 160–168. https://doi.org/10.1016/j.comptc.2010.12.016.

(22) Bixon, M.; Jortner, J. Intramolecular Radiationless Transitions. *J. Chem. Phys.* **1968**, *48* (2), 715–726. https://doi.org/10.1063/1.1668703.

(23) Shi, J.; Izquierdo, M. A.; Oh, S.; Park, S. Y.; Milián-Medina, B.; Roca-Sanjuán, D.;

Gierschner, J. Inverted Energy Gap Law for the Nonradiative Decay in Fluorescent Floppy Molecules: Larger Fluorescence Quantum Yields for Smaller Energy Gaps. *Org. Chem. Front.* **2019**, *6* (12), 1948–1954. https://doi.org/10.1039/C9QO00259F.

(24) Englman, R.; Jortner, J. The Energy Gap Law for Radiationless Transitions in Large Molecules. *Mol. Phys.* **1970**, *18* (2), 145–164. https://doi.org/10.1080/00268977000100171.

(25) Kwak, K.; Thanthirige, V. D.; Pyo, K.; Lee, D.; Ramakrishna, G. Energy Gap Law for Exciton Dynamics in Gold Cluster Molecules. *J. Phys. Chem. Lett.* **2017**, *8* (19), 4898–4905. https://doi.org/10.1021/acs.jpclett.7b01892.

(26) Caspar, J. V.; Meyer, T. J. Application of the Energy Gap Law to Nonradiative, Excited-State Decay. *J. Phys. Chem.* **1983**, *87* (6), 952–957. https://doi.org/10.1021/j100229a010.

(27) Kober, E. M.; Caspar, J. V; Lumpkin, R. S.; Meyer, T. J. Application of the Energy Gap Law to Excited-State Decay of Osmium(II)-Polypyridine Complexes: Calculation of Relative Nonradiative Decay Rates from Emission Spectral Profiles. *J. Phys. Chem.* **1986**, *90* (16), 3722–3734. https://doi.org/10.1021/j100407a046.

(28) Maciejewski, A.; Safarzadeh-Amiri, A.; Verrall, R. E.; Steer, R. P. Radiationless Decay of the Second Excited Singlet States of Aromatic Thiones: Experimental Verification of the Energy Gap Law. *Chem. Phys.* **1984**, *87* (2), 295–303. https://doi.org/10.1016/0301-0104(84)85054-5.

(29) Wilson, J. S.; Chawdhury, N.; Al-Mandhary, M. R. A.; Younus, M.; Khan, M. S.; Raithby, P. R.; Köhler, A.; Friend, R. H. The Energy Gap Law for Triplet States in Pt-Containing

Conjugated Polymers and Monomers. *J. Am. Chem. Soc.* **2001**, *123* (38), 9412–9417. https://doi.org/10.1021/ja010986s.

(30) Hochstrasser, R. M.; Marzzacco, C. Perturbations between Electronic States in Aromatic and Heteroaromatic Molecules. *J. Chem. Phys.* **1968**, *49* (3), 971–984. https://doi.org/10.1063/1.1670262.

(31) Zerbetto, F.; Zgierski, M. Z.; Orlandi, G.; Marconi, G. Vibronic Coupling in Polyenes and Their Derivatives. Interpretation of the Absorption and Emission Spectra of a Derivative of Dodecahexaene. *J. Chem. Phys.* **1987**, *87* (5), 2505–2512. https://doi.org/10.1063/1.453090.

(32) Russin, T. J.; Altinoğlu, E. İ.; Adair, J. H.; Eklund, P. C. Measuring the Fluorescent Quantum Efficiency of Indocyanine Green Encapsulated in Nanocomposite Particulates. *J. Phys. Condens. Matter* **2010**, *22* (33), 334217. https://doi.org/10.1088/0953-8984/22/33/334217.

(33) Rurack, K.; Spieles, M. Fluorescence Quantum Yields of a Series of Red and Near-Infrared Dyes Emitting at 600−1000 Nm. *Anal. Chem.* **2011**, *83* (4), 1232–1242. https://doi.org/10.1021/ac101329h.

(34) Ayala-Orozco, C.; Liu, J. G.; Knight, M. W.; Wang, Y.; Day, J. K.; Nordlander, P.; Halas, N. J. Fluorescence Enhancement of Molecules inside a Gold Nanomatryoshka. *Nano Lett.* **2014**, *14* (5), 2926–2933. https://doi.org/10.1021/nl501027j.

(35) Li, B.; Lu, L.; Zhao, M.; Lei, Z.; Zhang, F. An Efficient 1064 Nm NIR-II Excitation Fluorescent Molecular Dye for Deep-Tissue High-Resolution Dynamic Bioimaging.

Angew. Chemie Int. Ed. **2018**, *57* (25), 7483–7487. https://doi.org/10.1002/anie.201801226.

(36) Wang, S.; Fan, Y.; Li, D.; Sun, C.; Lei, Z.; Lu, L.; Wang, T.; Zhang, F. Anti-Quenching NIR-II Molecular Fluorophores for in Vivo High-Contrast Imaging and PH Sensing. *Nat. Commun.* **2019**, *10* (1), 1058. https://doi.org/10.1038/s41467-019-09043-x.

(37) Shi, Y.; Yuan, W.; Liu, Q.; Kong, M.; Li, Z.; Feng, W.; Hu, K.; Li, F. Development of Polyene-Bridged Hybrid Rhodamine Fluorophores for High-Resolution NIR-II Imaging. *ACS Mater. Lett.* **2019**, 418–424. https://doi.org/10.1021/acsmaterialslett.9b00265.

(38) Lei, Z.; Sun, C.; Pei, P.; Wang, S.; Li, D.; Zhang, X.; Zhang, F. Stable, Wavelength-Tunable Fluorescent Dyes in the NIR-II Region for In Vivo High-Contrast Bioimaging and Multiplexed Biosensing. *Angew. Chem. Int. Ed.* **2019**, *58* (24), 8166–8171. https://doi.org/10.1002/anie.201904182.

(39) Zhang, Fan; Li, Benhao; Zhao, M. Fluorescent Dye Excited/Emitted by Second Infrared Window and Preparation Method Thereof. CN 110079117, 2019.

(40) Hansch, C.; Leo, A.; Taft, R. W. *A Survey of Hammett Substituent Constants and Resonance and Field Parameters*; 1991; Vol. 91.

(41) Kasha, M.; Rawls, H. R.; El-Bayoumi, M. A. The Exciton Model In Molecular Spectroscopy. *Pure Appl. Chem.* **1965**. https://doi.org/10.1351/pac196511030371.

(42) Chen, W.; Cheng, C. A.; Cosco, E. D.; Ramakrishnan, S.; Lingg, J. G. P.; Bruns, O. T.; Zink, J. I.; Sletten, E. M. Shortwave Infrared Imaging with J-Aggregates Stabilized in Hollow Mesoporous Silica Nanoparticles. *J. Am. Chem. Soc.* **2019**, *141* (32), 12475–12480.

https://doi.org/10.1021/jacs.9b05195.

(43) Sun, C.; Li, B.; Zhao, M.; Wang, S.; Lei, Z.; Lu, L.; Zhang, H.; Feng, L.; Dou, C.; Yin, D.; Xu, H.; Cheng, Y.; Zhang, F. J-Aggregates of Cyanine Dye for NIR-II in Vivo Dynamic Vascular Imaging beyond 1500 Nm. *J. Am. Chem. Soc.* **2019**, *141* (49), 19221–19225. https://doi.org/10.1021/jacs.9b10043.

(44) Symes, R.; Sayer, R. M.; Reid, J. P. Cavity Enhanced Droplet Spectroscopy: Principles, Perspectives and Prospects. *Phys. Chem. Chem. Phys.* **2004**, *6* (3), 474–487. https://doi.org/10.1039/b313370b.

(45) Barnes, M. D.; Whitten, W. B.; Ramsey, J. M. Enhanced Fluorescence Yields through Cavity Quantum-Electrodynamic Effects in Microdroplets. *J. Opt. Soc. Am. B* **1994**, *11* (7), 1297. https://doi.org/10.1364/josab.11.001297.

(46) Lu, X.; Ye, G.; Punj, D.; Chiechi, R. C.; Orrit, M. Quantum Yield Limits for the Detection of Single-Molecule Fluorescence Enhancement by a Gold Nanorod. *ACS Photonics* **2020**, *7* (9), 2498–2505. https://doi.org/10.1021/acsphotonics.0c00803.

(47) G. Avramenko, A.; S. Rury, A. Quantum Control of Ultrafast Internal Conversion Using Nanoconfined Virtual Photons. *J. Phys. Chem. Lett.* **2020**, *11* (3), 1013–1021. https://doi.org/10.1021/acs.jpclett.9b03447.

(48) S. Ulusoy, I.; A. Gomez, J.; Vendrell, O. Modifying the Nonradiative Decay Dynamics through Conical Intersections via Collective Coupling to a Cavity Mode. *J. Phys. Chem. A* **2019**, *123* (41), 8832–8844. https://doi.org/10.1021/acs.jpca.9b07404.

(49) Humeniuk, A.; Mitrić, R.; Bonačić-Koutecký, V. Size Dependence of Non-Radiative Decay Rates in J-Aggregates. *J. Phys. Chem. A* **2020**, *124* (49), 10143–10151. https://doi.org/10.1021/acs.jpca.0c09074.

(50) Abe, T.; Miyazawa, A.; Konno, H.; Kawanishi, Y. Deuteration Isotope Effect on Nonradiative Transition of Fac-Tris (2-Phenylpyridinato) Iridium (III) Complexes. *Chem. Phys. Lett.* **2010**, *491* (4–6), 199–202. https://doi.org/10.1016/j.cplett.2010.03.084.

(51) Guttman, C.; Rice, S. A. Fluorescence Lifetimes of Individual Vibronic Levels of Partially Deuterated Benzenes: A Further Test of the Theory of Radiationless Processes. *J. Chem. Phys.* **1974**, *61* (2), 651–660. https://doi.org/10.1063/1.1681941.

(52) Kusinski, M.; Nagesh, J.; Gladkikh, M.; Izmaylov, A. F.; Jockusch, R. A. Deuterium Isotope Effect in Fluorescence of Gaseous Oxazine Dyes. *Phys. Chem. Chem. Phys.* **2019**, *21* (10), 5759–5770. https://doi.org/10.1039/c8cp05731a.

(53) Hirata, S.; Totani, K.; Watanabe, T.; Kaji, H.; Vacha, M. Relationship between Room Temperature Phosphorescence and Deuteration Position in a Purely Aromatic Compound. *Chem. Phys. Lett.* **2014**, *591*, 119–125. https://doi.org/10.1016/j.cplett.2013.11.019.

(54) Bai, L.; Sun, P.; Liu, Y.; Zhang, H.; Hu, W.; Zhang, W.; Liu, Z.; Fan, Q.; Li, L.; Huang, W. Novel Aza-BODIPY Based Small Molecular NIR-II Fluorophores for: In Vivo Imaging. *Chem. Commun.* **2019**, *55* (73), 10920–10923. https://doi.org/10.1039/c9cc03378e.

(55) Cooper, M.; Ebner, A.; Briggs, M.; Burrows, M.; Gardner, N.; Richardson, R.; West, R. *Cy3B TM : Improving the Performance of Cyanine Dyes*; 2004; Vol. 14.

(56) Sanborn, M. E.; Connolly, B. K.; Gurunathan, K.; Levitus, M. Fluorescence Properties and Photophysics of the Sulfoindocyanine Cy3 Linked Covalently to DNA. *J. Phys. Chem. B* **2007**, *111* (37), 11064–11074. https://doi.org/10.1021/jp072912u.

(57) Waggoner, A. S.; Mujumdar, R. B. Rigidized Trimethine Cyanine Dyes, 1998.

(58) Michie, M. S.; Götz, R.; Franke, C.; Bowler, M.; Kumari, N.; Magidson, V.; Levitus, M.; Loncarek, J.; Sauer, M.; Schnermann, M. J. Cyanine Conformational Restraint in the Far-Red Range. *J. Am. Chem. Soc.* **2017**, *139* (36), 12406–12409. https://doi.org/10.1021/jacs.7b07272.